THE JOURNAL OF PHYSICAL CHEMISTRY C
A JOURNAL OF THE AMERICAN CHEMICAL SOCIETY

pubs.acs.org/JPCC

Article

Au Nanoparticles Embedded in Carbon Self-Doping g-C_3N_4: Facile Photodeposition Method for Superior Photocatalytic H_2 Evolution

Published as part of The Journal of Physical Chemistry virtual special issue "Energy and Catalysis in China".

Lingfeng Li, Quan Zhang, Xiaohao Wang, Juhua Zhang, Huajun Gu, and Wei-Lin Dai*

Cite This: *J. Phys. Chem. C* 2021, 125, 10964−10973

Read Online

ABSTRACT: Developing an efficient and stable photocatalyst for photocatalytic H_2 production is of great significance for solving the existing energy and environmental crisis today. Herein, a superior photocatalyst, the uniformly dispersed ultrasmall Au nanoparticle (Au NP) decorated carbon self-doping g-C_3N_4 nanosheet (PDAu/CCNS), was successfully prepared via a simple photodeposition route. The as-prepared PDAu/CCNS displays a robust photocatalytic hydrogen (H_2) production activity (~15181 μmol h^{-1} g^{-1}) under visible-light irradiation. The above value is ~3 times higher than that of the neat carbon self-doping g-C_3N_4 (CCNS) (5330 μmol h^{-1} g^{-1}), ~2 times that of the impregnation Au NP decorated carbon self-doping g-C_3N_4 (IM-Au/CCNS) (9030 μmol h^{-1} g^{-1}), and ~50 times that of the bulk g-C_3N_4 (BCN) (300 μmol h^{-1} g^{-1}). The superior photocatalytic performance of the as-prepared PDAu/CCNS results from the evenly distributed ultrasmall Au NPs on CCNS, leading to a strong localized surface plasmon resonance (SPR) effect and an intimate contact between Au NPs and CCNS; thus, the as-prepared PDAu/CCNS exhibits a strong visible-light absorption and a high charge carrier separation and transfer rate, both of which synergistically promote the photocatalytic H_2 evolution process.

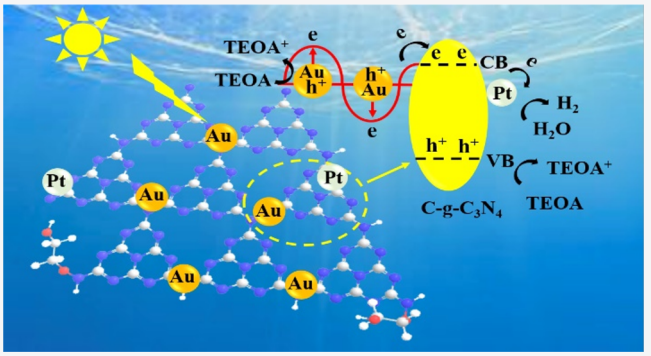

1. INTRODUCTION

Due to the increasingly aggravated energy and environmental crisis today, tremendous efforts have been made to develop new technologies to produce clean and renewable energy, among which the hydrogen (H_2) production via photocatalytic technology is believed to be one of the most potential technologies for these problems due to its ability to capture and utilize the exhaustless solar energy directly. To this end, numerous semiconductor photocatalysts have been developed in recent decades.[1−6] However, tremendous challenges remain to be tackled, such as the limited light absorption range (e.g., TiO_2, ZnO, $SrTiO_3$, Ta_2O_5, SnO_2), the fast photogenerated charge carrier recombination rate (e.g., α-Fe_2O_3, $BiVO_4$), a complicated preparation process, or a poor stability of materials (e.g., CdS, SnS_2, CdSe, Ni_2P, and InP), all of which hinder the practical application of photocatalysts.[6] Thus, it is of great significance to develop more suitable and efficient photocatalysts to solve the above problems.

Recently, as an organic semiconductor photocatalyst, polymeric graphitic carbon nitride (g-C_3N_4) has been widely studied due to its visible-light response ability, earth abundance, easy preparation, facile functionalization, excellent physicochemical stability, and suitable electronic band structure.[7] However, the high charge carrier recombination rate of g-C_3N_4 largely restrains its photocatalytic performance.[8−10] Moreover, the relatively wide band gap (~2.7 eV) of g-C_3N_4 limits its optical absorption range to the wavelengths shorter than 470 nm.[10,11] Thus, a large portion of visible light (~43% of incident sunlight) remains underutilized. To further expand the visible-light absorption range as well as accelerate the charge carrier separation and transmission rate of g-C_3N_4, thus improving its photocatalytic performance dramatically, tremendous studies have been carried out, such as the regulation of morphology and structure (e.g., thinner, ordered, porous, and highly crystalline g-C_3N_4), doping with metal elements,[12,13] or doping with nonmetal elements.[14−16] Besides, to compound with other materials (e.g., metals, semiconductors, carbons, and metal−organic frameworks) for the formation of g-C_3N_4 composite photocatalysts is also efficient to improve the photocatalytic performance.[7]

Plasmonic nanomaterials (e.g., Au, Ag, and Pt nanoparticles (NPs)) have gained tremendous interest to combine with

Received: March 13, 2021
Revised: April 22, 2021
Published: May 14, 2021

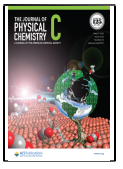

https://doi.org/10.1021/acs.jpcc.1c02269
J. Phys. Chem. C 2021, 125, 10964−10973

semiconductor photocatalysts for efficient photocatalytic performance[13,17−22] because of their unique shape and size-tunable localized surface plasmon resonance (SPR), among which the Au NPs were considered as promising candidates because of their excellent visible-light absorption, antioxidation, and corrosion resistance under various conditions.[10] Besides, it is proved that the modification of Au NPs on semiconductors like g-C_3N_4 can prolong the charge carrier lifetime of g-C_3N_4, thus significantly promoting its photocatalytic performance via acting as receivers to capture photogenerated electrons from g-C_3N_4. The SPR effect is greatly affected by the shape, size, and distribution of Au NPs. It has also been confirmed that the exposed facet of Au NPs can affect the photocatalytic performance dramatically, and the (111) facet-oriented Au NPs were proved to be in close contact with aromatic ring substrates, thus promoting the electron transfer rates dramatically.[23,24] Nevertheless, the traditional routes for the preparation of Au NPs, like impregnation,[25] coprecipitation,[26,27] ion exchange,[28] and chemical vapor deposition,[29] always undergo a complicated preparation process, leading to the as-prepared Au NPs with large particle sizes (>20 nm) and uncertain exposed facets randomly distributed on semiconductors, which are not favorable for the SPR effects and charge carrier transfer. By contrast, studies confirmed that the noble metal NPs (Ag, Pt, Au, etc.) can deposit on the electronic enrichment area of semiconductors precisely via a facile photodeposition route, thus realizing the position match, which would be favorable for the photogenerated charge carrier transfer, leading to the efficient and stable H_2 evolution.[30−32] Moreover, the morphology, size, and even the exposed facet of noble metal NPs can be easily controlled via the photodeposition method,[33] leading to the as-prepared noble metal NPs—semiconductors exhibit dramatically enhanced SPR effect, charge carrier transfer rate, and thus superior photocatalytic H_2 evolution performance.

In this work, ultrasmall Au NP decorated carbon self-doped g-C_3N_4 nanosheets (PDAu/CCNS) were obtained via a simple photodeposition route. The reason why we chose CCNS instead of BCN is due to the fact that the CCNS is much more ordered and highly crystalline. Besides, the CCNS exhibits a much larger specific surface area and a better conductivity due to the carbon doping. Moreover, the self-doping carbon could play a significant role when connecting with Au NPs because of the electron deficiency of the self-doping carbon and the electron richness of Au NPs. Consequently, the as-prepared PDAu/CCNS exhibits excellent visible-light absorption and charge carrier separation and transfer rate because of the strong SPR effect and the intimate contact between the ultrasmall Au NPs and CCNS, both of which synergistically promote the photocatalytic H_2 evolution process. Thus, the PDAu/CCNS displays a superior photocatalytic H_2 evolution performance (∼15181 μmol h^{-1} g^{-1}) under visible-light irradiation, which is ∼3 times that of the neat carbon self-doping g-C_3N_4 (CCNS) (∼5330 μmol h^{-1} g^{-1}), ∼2 times that of the Au NP decorated carbon self-doping g-C_3N_4 derived from the conventional impregnation method (IM-Au/CCNS) (∼9030 μmol $h^{-1}g^{-1}$), and ∼50 times that of bulk g-C_3N_4(BCN) obtained from direct thermal polycondensation of melamine. Moreover, the photocatalytic activity of PDAu/CCNS exhibits no evident decrease after a continuous photocatalytic H_2 evolution test for 40 h (15 runs) under visible-light (λ > 400 nm) irradiation. In addition, the QE of the PDAu/CCNS over the wavelength of 420 and 550 nm reaches up to 10.5% and 5.5%, respectively, demonstrating its excellent visible-light utilization.

2. METHODS

2.1. Synthesis of Photocatalysts. CCNS and BCN: The CCNS was prepared according to our previous work,[34] and the BCN was obtained via direct thermal polymerization of a certain amount of melamine in a tube furnace filled with N_2 and kept at 550 °C for 3 h under the atmosphere, with a 5 °C min^{-1} heating rate.

IM-Au/CCNS: The IM-Au/CCNS was prepared via a reported impregnation method.[35] Briefly, 0.1 g of CCNS was added in a two-necked round-bottom flask containing 100 mL of deionized water and was well dispersed by ultrasonication, and then 0.042 mol of urea was added in this mixture as well. After that, a certain amount of $HAuCl_4{\cdot}4H_2O$ aqueous solution was added to the above solution until the content of Au was 0.6 wt %. The above flask was covered to prevent the $HAuCl_4{\cdot}4H_2O$ from decomposing under sunlight. Then, the flask was kept stirring for 4 h at 80 °C. Afterward, the solution was filtered and dried in an oven overnight. Finally, it was calcined again in a muffle furnace at 300 °C for 2 h.

PDAu/CCNS and PDAu/BCN: The PDAu/CCNS was prepared by the photodeposition method. Typically, 0.02 g of CCNS was well dispersed in 100 mL of aqueous solution containing 10 vol % of triethanolamine sacrificial agent, which was contained in a 400 mL vessel. After that, a certain amount of $HAuCl_4{\cdot}4H_2O$ was added with the content of Au being 0.6 wt % for the in situ deposition of ultrasmall Au NPs on CCNS. Then the vessel was sealed and evacuated to exhaust the air inside. After that, the above solution was irradiated by a 300 W Xe lamp (Ceaulight, CEL-HXF300) equipped with a cutoff filter of 400 nm as visible light for 5 min to trigger the photodeposition. The photodeposition parameters on the photocatalytic activities of PDAu/CCNS during visible-light-driven water splitting were optimized for the optimal photocatalytic H_2 production performance (Figure S2), including the addition of Au (0.4, 0.6, and 1.0 wt % under the same photodeposition time of 5 min, which were labeled as 0.4% PDAu/CCNS, 0.6% PDAu/CCNS, and 1.0% PDAu/CCNS, respectively) and the photodeposition time (2.5, 5.0, 10, 20, and 30 min with the same addition of 0.6 wt % of Au, which were designed as PDAu/CCNS-2.5, PDAu/CCNS-5.0, PDAu/CCNS-10, PDAu/CCNS-20, and PDAu/CCNS-30, respectively). Furthermore, the effects of photodeposition time on the morphology and size of Au NPs and thus the corresponding impact on optical absorption and charge carrier separation properties for PDAu/CCNS-2.5, PDAu/CCNS-10, and PDAu/CCNS-30 were also studied as shown in Figure S3 and Figure S4. Besides, to aid comparison, the PDAu/BCN was also prepared under the same preparation conditions with PDAu/CCNS except that the CCNS was replaced by the BCN.

2.2. Characterization, Photoelectrochemical, and Photocatalytic Performance Tests. Detailed characterization, photoelectrochemical, and photocatalytic performance tests are elaborated in the Supporting Information.

3. RESULTS AND DISCUSSION

3.1. Structure, Morphology, and Composition. The XRD pattern was obtained to investigate the crystal structure. The typical g-C_3N_4 diffraction peaks are found for all samples

https://doi.org/10.1021/acs.jpcc.1c02269
J. Phys. Chem. C 2021, 125, 10964−10973

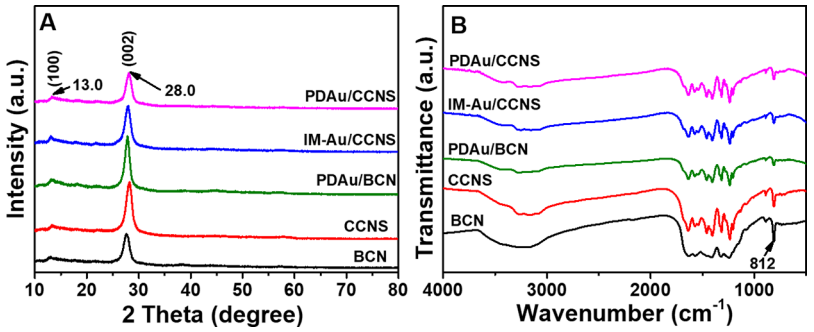

Figure 1. XRD patterns (A) and FT-IR spectra (B) of BCN, CCNS, PDAu/BCN, IM-Au/CCNS, and PDAu/CCNS.

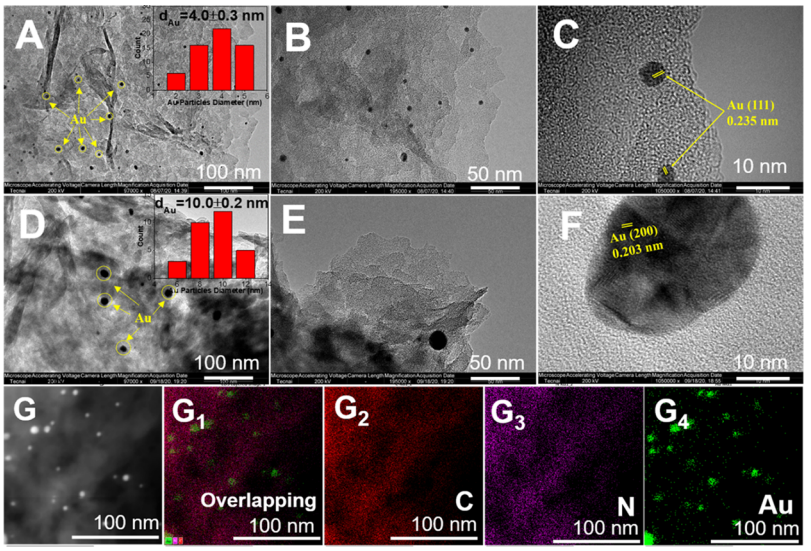

Figure 2. TEM images of PDAu/CCNS (A, B) and IM-Au/CCNS (D, E). The insets in A and D displayed the corresponding diameter distribution of Au NPs on PDAu/CCNS and IM-Au/CCNS; HRTEM images of PDAu/CCNS (C) and IM-Au/CCNS (F); HAADF-STEM of PDAu/CCNS (G) and the corresponding elemental mappings for overlapping of C, N, and Au (G_1), C (G_2), N (G_3), and Au (G_4) elements.

(Figure 1A). Briefly, the weaker peak located at around 13.0° is ascribed to the (100) peak, which corresponded to the in-plane structural packing motif of the tri-*s*-triazine units in g-C_3N_4, and the stronger peak at around 28.0° is ascribed to a typical (002) peak, which corresponded to the interlayer stacking of aromatic segments of g-C_3N_4.[36−38] It is noticeable that the characteristic diffraction peak of Au was not evident in PDAu/BCN, IM-Au/CCNS, and PDAu/CCNS, due to the low content and high dispersion of Au NPs. Besides, FT-IR was also conducted to get the structural information for different samples (Figure 1B). All samples exhibit typical g-C_3N_4 FT-IR spectra. In detail, the broad band ranges from 3000 to 3600 cm^{-1} are attributed to the surface-adsorbed hydroxyl or the $-NH_2$ group stretching vibration modes. The peaks located at about the 1200−1700 cm^{-1} region can be ascribed to the typical stretching vibration peaks of sp^2 C═N. The intense peak at around 812 cm^{-1} is attributed to the characteristic out-of-plane skeletal bending modes of the *s*-triazine units.[39] Generally, the Au−O vibration absorption peak was located at about 818 cm^{-1}. However, no Au−O vibration peak was observed from the FT-IR spectra of PDAu/BCN, IM-Au/CCNS, and PDAu/CCNS, indicating that the Au−O vibration peak may be covered by the breathing mode of the *s*-triazine units at 812 cm^{-1}.[40]

To further compare the nanostructure of Au NPs prepared by photodeposition and impregnation on CCNS, the TEM (insets show the corresponding diameter distribution of Au NPs) images of PDAu/CCNS and IM-Au/CCNS were obtained as shown in Figure 2(A, B) and (D, E). It can be found that the ultrasmall Au NPs (~4 nm) are evenly distributed on CCNS via the photodeposition method (Figure 2A,B). However, the Au NPs are much larger and unevenly deposited on CCNS with the average size reaching up to 10.0 nm via the impregnation route (Figure 2D,E). Besides, the HRTEM images for PDAu/CCNS and IM-Au/CCNS are obtained and shown in Figure 2(C and F) to further study the corresponding microstructures of Au NPs. The Au NPs of PDAu/CCNS exhibit clear lattice fringes of ca. 0.235 nm,[41,42] which are attributed to metallic Au (111), whereas the Au NPs of IM-Au/CCNS exhibit lattice fringes of ca. 0.203 nm, which are ascribed to metallic Au (200). This result indicates that the photodeposition method is more favorable for the preparation of uniformly dispersed (111) facet-oriented ultrasmall Au NPs on CCNS, which can result in a strong SPR effect and a strong coupling between Au NPs and CCNS, leading to the as-obtained PDAu/CCNS exhibiting dramatically enhanced optical absorption and charge carrier transfer rate, as well as its improved photocatalytic property. However, the impregnation method is inclined to obtain much larger and unevenly distributed (200)-facet-oriented Au NPs on CCNS, resulting in a relatively poor SPR effect and weak contact between Au NPs and CCNS, thus making the IM-Au/CCNS exhibit a

https://doi.org/10.1021/acs.jpcc.1c02269
J. Phys. Chem. C 2021, 125, 10964−10973

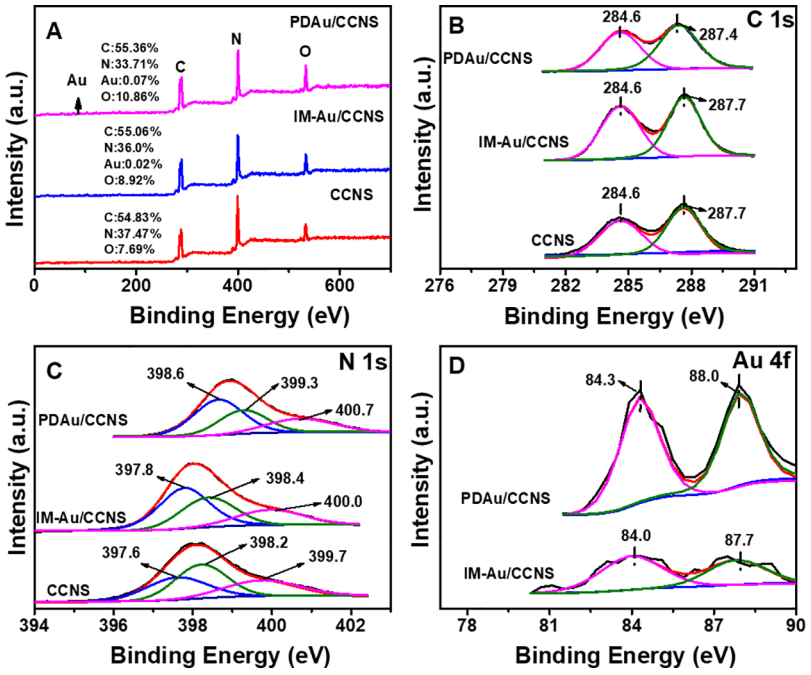

Figure 3. XPS spectra (A) and high-resolution C 1s (B), N 1s (C), and Au 4f (D) XPS spectra of CCNS, IM-Au/CCNS, and PDAu/CCNS.

relatively lower photocatalytic performance than PDAu/CCNS. To further verify the uniformly dispersed ultrasmall Au NPs on PDAu/CCNS, HAADF-STEM and the corresponding elemental mapping images of PDAu/CCNS were displayed in Figure 2(G–G_4). Both C, N, and ultrasmall Au NPs were evenly distributed over PDAu/CCNS, demonstrating that the ultrasmall Au NPs were successfully deposited on CCNS via the simple photodeposition route. Moreover, the elemental compositions of CCNS, IM-Au/CCNS, and PDAu/CCNS by STEM-EDX were listed in Table S1. The Au atomic concentration of PDAu/CCNS reaches up to 0.16% but only 0.06% for IM-Au/CCNS, demonstrating that the photodeposition is much more efficient than impregnation for the modification of Au NPs on CCNS for superior photocatalytic performance. Also, the TEM images and the corresponding diameter distribution of Au NPs for PDAu/CCNS-2.5, PDAu/CCNS-5, and PDAu/CCNS-30 were compared to investigate the effects of photodeposition time on the morphology and size of Au NPs during the photodeposition process (shown in Figure S3). As demonstrated in Figure S3, the uniformly dispersed ultrasmall Au NPs (~4 nm) can only be obtained at a moderate photodeposition time (~5.0 min in this work). In other words, too short and too long photodeposition times are not favorable for the formation of uniformly dispersed ultrasmall Au NPs. In details, when the photodeposition times are too short (like 2.5 min), nearly half of the as-formed Au NPs are too small (~2.0 nm), and most of the others are ~5.5 nm in diameter, though the average size is also ~4.0 nm, demonstrating that the diameter distribution of Au NPs for PDAu/CCNS-2.5 is extremely uneven. Meanwhile, when the photodeposition times are greatly extended to 30 min, parts of the as-formed Au NPs grew too large, with a diameter of ~12.0 nm, which may not be favorable for the SPR effect and charge carrier transfer between Au NPs and CCNS.

To further investigate the surface elemental composition and their oxidation states of CCNS, IM-Au/CCNS, and PDAu/CCNS, the XPS survey and the corresponding high-resolution C 1s, N 1s, and Au 4f XPS spectra were obtained as displayed in Figure 3. The C 1s, N 1s, and O 1s peaks can be clearly observed for CCNS, IM-Au/CCNS, and PDAu/CCNS (Figure 3A). The emergence of the O 1s peak results from the surface-adsorbed hydroxyl groups (–OH) of the as-prepared catalysts,[35] whereas the Au 4f peaks were not evident for both IM-Au/CCNS and PDAu/CCNS, due to the low content of Au NPs (the Au atomic percentage was determined to be 0.02% and 0.07%, respectively, for IM-Au/CCNS and PDAu/CCNS by XPS). The lower Au content but larger Au NP sizes in IM-Au/CCNS than that in PDAu/CCNS indicates that the Au NPs prepared by impregnation are inclined to agglomerate, leading to the as-obtained Au NPs with large sizes, which may not be favorable for a strong SPR effect. Besides, the high-resolution C 1s spectra were also obtained (shown in Figure 3B). For CCNS and IM-Au/CCNS, two peaks were well fitted at the binding energies of 284.6 and 287.7 eV, which were derived from the carbon atom in C–C/C=C and N=C–N of g-C_3N_4.[43] Moreover, the peak of N=C–N for PDAu/CCNS slightly shifted to 287.4 eV, which can be ascribed to strong coupling between the (111) facets of Au NPs and CCNS for PDAu/CCNS, and this kind of intense interaction is very conducive to the photoinduced charge carrier transfer between Au NPs and CCNS. Besides, the high-resolution N 1s spectra of CCNS, IM-Au/CCNS, and PDAu/CCNS were also obtained (Figure 3C). The high-resolution N 1s of CCNS was well fitted with three peaks at binding energies of 397.6, 398.2, and 399.7 eV, respectively,[44] corresponding to the C–N=C, N–(C_3), and N–H of g-C_3N_4.[45,46] By comparison, the high-resolution N 1s peaks of IM-Au/CCNS and PDAu/CCNS shifted toward higher binding energy (397.8, 398.4, 400.0 eV and 398.6, 399.3, and 400.7 eV, respectively, for IM-Au/CCNS and PDAu/CCNS), which can be ascribed to the interaction between the Au NPs and CCNS. The more obvious N 1s peak shifts for PDAu/CCNS than IM-Au/CCNS demonstrate the stronger interaction between the (111) facets of Au NPs and CCNS in

https://doi.org/10.1021/acs.jpcc.1c02269
J. Phys. Chem. C 2021, 125, 10964–10973

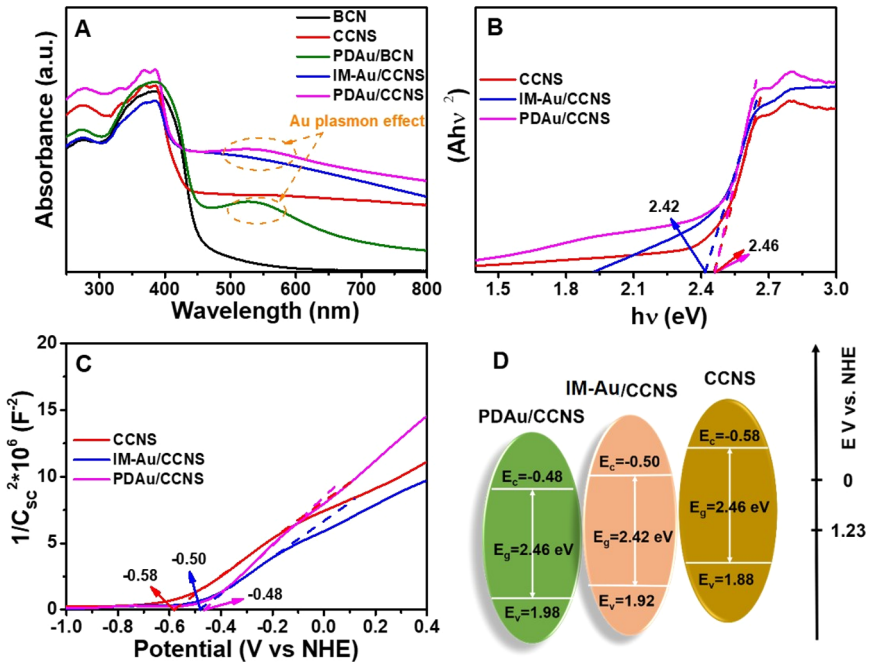

Figure 4. UV−vis DRS spectra of BCN, CCNS, PDAu/BCN, IM-Au/CCNS, and PDAu/CCNS (A), the corresponding Tauc plots (B), the Mott−Schottky plots (C), and schematic energy level structures (D) for CCNS, IM-Au/CCNS, and PDAu/CCNS.

PDAu/CCNS certainly. Then, Figure 3D displays the high-resolution Au 4f spectra for IM-Au/CCNS and PDAu/CCNS, both of which exhibit two peaks well fitted at binding energies of ca. 84.0 (Au $4f_{7/2}$) and ca. 88.0 eV (Au $4f_{5/2}$),[47,48] demonstrating the presence of Au NPs for both IM-Au/CCNS and PDAu/CCNS. The results were also supported by the HRTEM images (Figure 2C). Moreover, the stronger Au 4f peaks for PDAu/CCNS certify the higher surface content of Au NPs. The higher binding energy of Au $4f_{7/2}$ for PDAu/CCNS (84.3 eV) than IM-Au/CCNS (84.0 eV) also indicates the stronger interaction between the Au NPs (111) and CCNS for PDAu/CCNS than the Au NPs (200) and CCNS for IM-Au/CCNS. This finding is in line with the XRD and TEM results.

3.2. Optical Properties, Band Structures, and Charge Carrier Separation Performance. To compare the optical absorption properties of BCN, CCNS, PDAu/BCN, IM-Au/CCNS, and PDAu/CCNS, the UV−vis DRS spectra for different samples were obtained as presented in Figure 4A. For the BCN, apparent absorption can only be observed in the range of 250−450 nm, whereas the CCNS exhibited much enhanced absorption at wavelengths longer than 450 nm, which is derived from the carbon self-doping as demonstrated in our previous work.[34] By contrast, PDAu/BCN, IM-Au/CCNS, and PDAu/CCNS displayed additional shoulder absorption peaks at around 530 nm, which were derived from the SPR effects of the surface-deposited Au NPs on BCN and CCNS. Moreover, both IM-Au/CCNS and PDAu/CCNS exhibited much enhanced visible-light absorption (λ > 420 nm) compared to PDAu/BCN, due to the synergistic effects of the carbon self-doping and the SPR effects of Au NPs on IM-Au/CCNS and PDAu/CCNS. By comparison, the PDAu/CCNS still possessed a more substantial SPR effect and thus a stronger visible-light absorption than IM-Au/CCNS, demonstrating that the photodeposition method was more favorable than impregnation to decorate strong SPR Au NPs on CCNS, thus producing more charge carriers for photocatalytic H_2 evolution. In addition, the optical absorption properties for PDAu/CCNS-2.5 and PDAu/CCNS-30 were also compared with PDAu/CCNS through the UV−vis DRS spectra (Figure S4A). The PDAu/CCNS exhibited a much stronger SPR effect and thus much enhanced optical absorption within the visible-light region than PDAu/CCNS-2.5 and PDAu/CCNS-30. This finding demonstrated that the PDAu/CCNS with uniformly dispersed ultrasmall Au NPs (∼4 nm) would be more conducive to the photocatalytic H_2 evolution.

To further investigate the effects of Au NPs on the energy band structures of CCNS by photodeposition and impregnation, the corresponding Tauc and Mott−Schottky plots for CCNS, IM-Au/CCNS, and PDAu/CCNS were obtained as presented in Figure 4(B and C). From the Tauc plots (Figure 4B), the band gaps of CCNS, IM-Au/CCNS, and PDAu/CCNS were calculated to be 2.46, 2.42, and 2.46 eV, respectively. In addition, the Fermi levels (E_f) were determined as −0.58, −0.50, and −0.48 V vs NHE for CCNS, IM-Au/CCNS, and PDAu/CCNS by extrapolating the Mott−Schottky plots (Figure 4C) to $1/C^2 = 0$. Consequently, the band structures for CCNS, IM-Au/CCNS, and PDAu/CCNS are schematically illustrated in Figure 4D. It is worth noting that both the conduction band level (E_c = −0.48 V vs NHE) and the valence band level (E_v = 1.98 V vs NHE) of PDAu/CCNS moved slightly toward the positive directions compared with that of CCNS (E_c = −0.58 and E_v = 1.88 V vs NHE) and IM-Au/CCNS (E_c = −0.50 and E_v = 1.92 V vs NHE), indicating that the oxidation ability of PDAu/CCNS slightly increased while the reducing ability slightly decreased. However, this tiny shortcoming of PDAu/CCNS cannot conceal the advantages of its dramatically enhanced visible light absorption and charge carrier separation and transfer rate, which were derived from the strong localized SPR effect and the intimate contact between the ultrasmall Au NPs and the CCNS; thus, the PDAu/CCNS can still exhibit an excellent photocatalytic H_2 evolution performance.

https://doi.org/10.1021/acs.jpcc.1c02269
J. Phys. Chem. C 2021, 125, 10964−10973

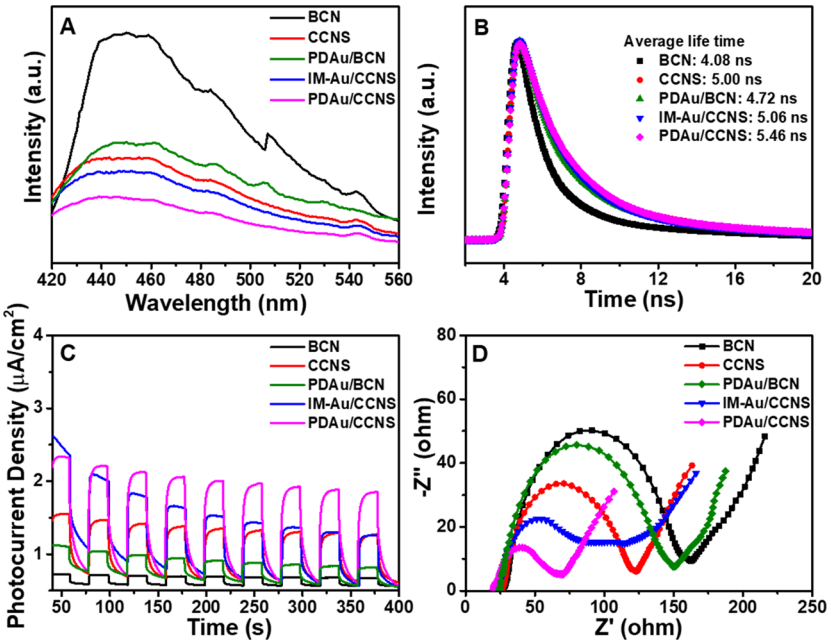

Figure 5. PL emission spectra (λ_{ex} = 400 nm) (A), time-resolved PL spectra (λ_{ex} = 375 nm) (B), photocurrent responses (C), and EIS Nyquist plots (D) for BCN, CCNS, PDAu/BCN, IM-Au/CCNS, and PDAu/CCNS.

To investigate the photoinduced electron−hole pair transfer and separation efficiency, the PL emission spectra, time-resolved PL spectra, transient photocurrent responses, and EIS profile for BCN, CCNS, PDAu/BCN, IM-Au/CCNS, and PDAu/CCNS were obtained and displayed in Figure 5. All samples displayed an intrinsic PL emission peak with optical energy close to their band gaps (~440 nm) (Figure 5A), and the BCN exhibits the strongest emission peaks centered around 450 nm, indicating the highest charge carrier recombination rates. CCNS, PDAu/BCN, IM-Au/CCNS, and PDAu/CCNS displayed greatly decreased PL intensities, suggesting their significantly improved charge carrier separation rates. Among these, the PDAu/CCNS exhibits much lower PL emission intensities than IM-Au/CCNS and CCNS, indicating its efficient charge carrier separation rate. The result demonstrates the vital roles of the photodeposition-derived Au NPs in promptly transferring the photogenerated electrons from CCNS, thus inhibiting the charge carrier recombination, which results from the strong interaction between the (111) facet-oriented and CCNS.[49] Figure S4B displayed the PL emission spectra for PDAu/CCNS-2.5, PDAu/CCNS-5, and PDAu/CCNS-30, from which the PDAu/CCNS exhibited a dramatically decreased PL emission intensity compared with PDAu/CCNS-2.5 and PDAu/CCNS-30, demonstrating the most efficient charge carrier separation and transfer rates in PDAu/CCNS-5. Figure 5B displayed the time-resolved fluorescence decay spectra for BCN, CCNS, PDAu/BCN, IM-Au/CCNS, and PDAu/CCNS to help study the photogenerated charge carrier lifetimes, and Table S2 listed the corresponding fitted parameters. The PDAu/CCNS exhibits the longest average fluorescence lifetime (τ = 5.46 ns) compared with all the others, including BCN (τ = 4.08 ns), CCNS (τ = 5.00 ns), PDAu/BCN (τ = 4.72 ns), and IM-Au/CCNS (τ = 5.06 ns), indicating the lowest charge carrier recombination rate in PDAu/CCNS, which matches well with the PL emission spectra results (Figure 5A). Furthermore, the transient photocurrents were also measured for all samples to investigate further the photogenerated electron−hole pair separation and transmission efficiency (as presented in Figure 5C). Clearly, the PDAu/CCNS exhibits a much higher photocurrent density than other samples irradiated via visible light, of which the average values are 2.0, 1.4, 1.3, 0.9, and 0.7 μA/cm^2, respectively, for PDAu/CCNS, IM-Au/CCNS, CCNS, PDAu/BCN, and BCN. The highest photocurrent in PDAu/CCNS manifests the most efficient photoinduced charge carrier separation in it, which is consistent with the above PL and time-resolved PL results. Moreover, the EIS profile was also recorded for all samples, as displayed in Figure 5D. Generally, charge carrier transfer resistance is positively correlated with the arc radius. That is, a smaller arc radius signifies a faster charge transfer rate. The arc radius order is PDAu/CCNS < IM-Au/CCNS < CCNS < PDAu/BCN < BCN, indicating that the PDAu/CCNS has the fastest charge carrier separation and transmission rate, thus resulting in its superior photocatalytic performance. All the above results demonstrated that the modification of uniformly dispersed ultrasmall Au NPs with a (111) facet exposed on CCNS via the photodeposition method can promote the optical absorption as well as accelerate the charge carrier transfer rate dramatically, due to the strong SPR effect and the intimate contact between the photodeposition prepared Au NPs and CCNS, thus leading to its excellent photocatalytic H_2 production performance. The transient photocurrents and EIS for PDAu/CCNS-2.5, PDAu/CCNS-5, and PDAu/CCNS-30 were also compared, as shown in Figure S4(C and D). The PDAu/CCNS-5 exhibited a larger photocurrent density and a smaller EIS arc radius than both PDAu/CCNS-2.5 and PDAu/CCNS-30, demonstrating a more efficient charge carrier separation and transfer rate in PDAu/CCNS, which verified again that the PDAu/CCNS-5 with uniformly dispersed ultrasmall Au NPs (~4 nm) could be more efficient for photocatalytic H_2 evolution.

3.3. Photocatalytic Performance. The photocatalytic performance of BCN, CCNS, PDAu/BCN, IM-Au/CCNS,

https://doi.org/10.1021/acs.jpcc.1c02269
J. Phys. Chem. C 2021, 125, 10964−10973

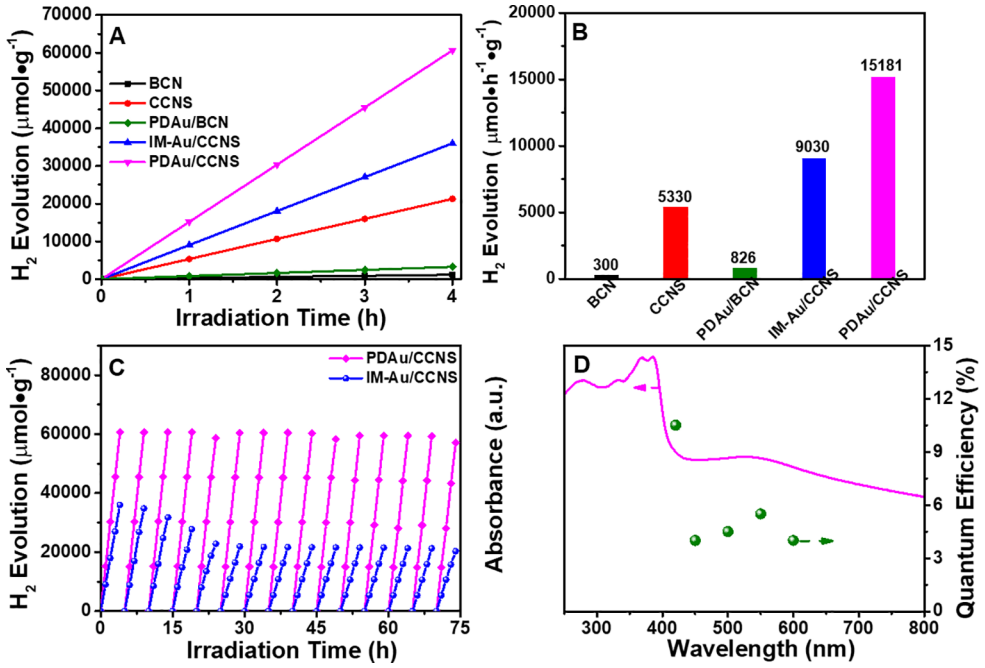

Figure 6. (A) Photocatalytic H_2 production and (B) the average H_2 evolution rates of BCN, CCNS, PDAu/BCN, IM-Au/CCNS, and PDAu/CCNS; (C) the stable H_2 evolution; and (D) QE of PDAu/CCNS under different visible-light irradiation.

and PDAu/CCNS was evaluated via the photocatalytic H_2 evolution performance irradiated with visible light (λ > 400 nm). The H_2 production almost linearly increases with the reaction time for all the samples (Figure 6A), demonstrating that BCN, CCNS, PDAu/BCN, IM-Au/CCNS, and PDAu/CCNS possessed obvious photostability. Then, the corresponding average photocatalytic H_2 evolution rates for BCN, CCNS, PDAu/BCN, IM-Au/CCNS, and PDAu/CCNS were further calculated and presented in Figure 6B. Obviously, the PDAu/CCNS presents the highest average H_2 production rate with a value reaching up to 15 181 μmol g^{-1} h^{-1}. However, the values for BCN, PDAu/BCN, CCNS, and IM-Au/CCNS are only 300, 826, 5330, and 9030 μmol g^{-1} h^{-1}, respectively. In other words, the photocatalytic H_2 production rate for PDAu/CCNS is nearly 50, 18, 3, and 2.0 times higher than that of BCN, PDAu/BCN, CCNS, and IM-Au/CCNS, manifesting its superior photocatalytic H_2 evolution performance. Moreover, the photocatalytic H_2 evolution stability was also investigated for PDAu/CCNS (Figure 6C). Consequently, the PDAu/CCNS displays a linear yield of H_2 under 4 h continuous irradiation. Moreover, the H_2 production value for PDAu/CCNS shows no significant decline after 15 cycles, which demonstrates its superior stability. Furthermore, the structure, morphology, and elemental composition of the reused PDAu/CCNS were also investigated by XRD, TEM, HRTEM, HAADF-STEM, STEM-EDX, and XPS to study the stability of PDAu/CCNS (as shown in Figure S5, Figure S6, Figure S7, and Table S1). No noticeable change can be found from the XRD patterns of the reused PDAu/CCNS after cycles of reaction (Figure S5), indicating the excellent crystal structural stability of PDAu/CCNS. Moreover, ultrasmall Au NPs (~4 nm) are still evenly dispersed on CCNS with a minimal amount of Au NPs grown to 9 nm, and thus, the average diameter slightly increased to ~5.0 nm (Figure S6A). The Au NPs still exhibit clear lattice fringes of ca. 0.235 nm (Figure S6B), and the C, N, and ultrasmall Au NPs are still evenly distributed over PDAu/CCNS (Figure S6(C−C4)). Besides, no obvious changes can be observed in Au NPs from the XPS spectra (Figure S7A) and high-resolution Au 4f XPS spectra (Figure S 7B) of recycled PDAu/CCNS. All the above results demonstrate the superior morphology and structural and compositional stability of PDAu/CCNS. Moreover, the Au atomic concentration of the reused PDAu/CCNS (0.15%) exhibits no evident decrease compared with the fresh PDAu/CCNS (0.16%) (shown in Table S1), certifying the robust stability of PDAu/CCNS again. The quantum efficiency (QE) of PDAu/CCNS under different visible-light irradiation (including λ = 420, 450, 500, 550, and 600 nm) was also calculated to better illustrate the SPR effect of Au NPs (as displayed in Figure 6D), from which the QE value of PDAu/CCNS reaches ~10.5% and 5.5%, respectively, under λ of 420 and 550 nm monochromatic light irradiation. Moreover, the QE of PDAu/CCNS shows a relatively consistent trend with the light absorption, demonstrating that light absorption plays a significant role in the photocatalytic performance of PDAu/CCNS. Thus, the decoration of the ultrasmall Au NPs with strong SPR effect and visible-light absorption on PDAu/CCNS could promote the photocatalytic H_2 evolution performance of PDAu/CCNS significantly. Besides, several reported g-C_3N_4 materials with high QE and H_2 evolution rate were also summarized in Table S3, from which the as-prepared PDAu/CCNS exhibits excellent photocatalytic performance, demonstrating its relatively superior visible-light utilization.

The photocatalytic H_2 evolution process of PDAu/CCNS was displayed in Scheme 1. When visible light (λ > 400 nm) was irradiated on PDAu/CCNS, photogenerated electron−hole pairs were generated by CCNS. Meanwhile, several hot electrons generated from the plasmon effect of Au NPs can also transfer from Au NPs to the conduction band of CCNS. Then, the electrons were further transferred from the conduction band of CCNS to the added Pt cocatalysts to produce H_2 via water splitting. Meanwhile, the holes left in Au NPs and the valence band of CCNS were rapidly consumed by

https://doi.org/10.1021/acs.jpcc.1c02269
J. Phys. Chem. C 2021, 125, 10964−10973

Scheme 1. Illustration of the Photocatalytic H_2 Evolution Process of PDAu/CCNS

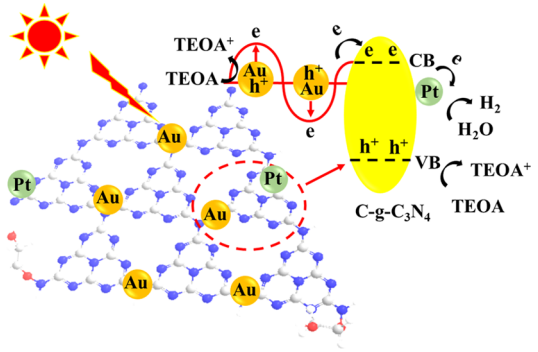

the added TEOA sacrificial agent. Thus, a stable photocatalytic H_2 evolution process was achieved.

4. CONCLUSIONS

In summary, a facile photodeposition method was carried out to prepare a robust ultrasmall Au NP decorated carbon self-doped g-C_3N_4 nanosheet photocatalyst. The as-prepared PDAu/CCNS exhibits a superior photocatalytic hydrogen evolution performance (~15181 μmol h^{-1} g^{-1}) under visible-light irradiation, which is ~3 times that of the neat carbon self-doping g-C_3N_4 (~5330 μmol h^{-1} g^{-1}), ~2 times that of the Au NP decorated CCNS derived from the conventional impregnation method (~9030 μmol h^{-1} g^{-1}), and ~50 times that of bulk g-C_3N_4 (300 μmol h^{-1} g^{-1}). The superior photocatalytic activity of PDAu/CCNS results from the evenly dispersed ultrasmall Au NPs with the (111) facet exposed on CCNS, leading to a strong SPR effect and an intimate contact between the ultrasmall Au NPs and CCNS; thus, an enhanced visible-light absorption and an accelerated charge carrier transfer rate were obtained, both of which synergistically promoted the photocatalytic process of PDAu/CCNS. This work demonstrates that photodeposition is a feasible route for the decoration of a strong SPR effect of ultrasmall metal Au NPs on semiconductor photocatalysts. Besides, a strong coupling between metal NPs and semiconductors can be achieved via the photodeposition route. Thus, the light absorption and charge carrier separation and transfer rate of semiconductors can be significantly improved for efficient photocatalytic utilization.

■ ASSOCIATED CONTENT

Supporting Information

The Supporting Information is available free of charge at https://pubs.acs.org/doi/10.1021/acs.jpcc.1c02269.

Materials, characterization, photoelectrochemical measurement, photocatalytic activity tests, clear HRTEM image of Au nanoparticles of PDAu/CCNS and IM-Au/CCNS (Figure S1); average photocatalytic H_2 evolution rates for PDAu/CCNS prepared under different addition of Au and different photodeposition time (Figure S2); TEM images and the corresponding diameter distribution of Au NPs for PDAu/CCNS prepared under different photodeposition time (Figure S3); UV−vis, DRS spectra, PL emission spectra, photocurrent responses, and EIS Nyquist plots for PDAu/CCNS prepared under different photodeposition times (Figure S4); XRD patterns of the fresh and recycled PDAu/CCNS (Figure S5); TEM, HRTEM, and HAADF-STEM for reused PDAu/CCNS (Figure S6); XPS survey spectra and high-resolution Au 4f XPS spectra of the fresh and recycled PDAu/CCNS (Figure S7); elemental composition of samples by STEM-EDX (Table S1); fluorescence emission lifetime and relevant data fitted by a two-exponential function (Table S2); and summary of g-C_3N_4 reported with high QE and H_2 evolution rate (Table S3) (PDF)

■ AUTHOR INFORMATION

Corresponding Author

Wei-Lin Dai − *Department of Chemistry and Shanghai Key Laboratory of Molecular Catalysis and Innovative Materials, Fudan University, Shanghai 200433, P. R. China;* orcid.org/0000-0003-4838-5678; Phone: +86 3124 9122; Email: wldai@fudan.edu.cn; Fax: +86 3124 2978

Authors

Lingfeng Li − *Department of Chemistry and Shanghai Key Laboratory of Molecular Catalysis and Innovative Materials, Fudan University, Shanghai 200433, P. R. China*

Quan Zhang − *Department of Chemistry and Shanghai Key Laboratory of Molecular Catalysis and Innovative Materials, Fudan University, Shanghai 200433, P. R. China*

Xiaohao Wang − *Department of Chemistry and Shanghai Key Laboratory of Molecular Catalysis and Innovative Materials, Fudan University, Shanghai 200433, P. R. China*

Juhua Zhang − *Department of Chemistry and Shanghai Key Laboratory of Molecular Catalysis and Innovative Materials, Fudan University, Shanghai 200433, P. R. China*

Huajun Gu − *Department of Chemistry and Shanghai Key Laboratory of Molecular Catalysis and Innovative Materials, Fudan University, Shanghai 200433, P. R. China*

Complete contact information is available at: https://pubs.acs.org/10.1021/acs.jpcc.1c02269

Notes

The authors declare no competing financial interest.

■ ACKNOWLEDGMENTS

This work was financially supported by the Natural Science Foundation of Shanghai (19ZR1403500), the National Natural Science Foundation of China (NNSFC, Project 21373054), and the Natural Science Foundation of Shanghai Science and Technology Committee (08DZ2270500).

■ REFERENCES

(1) Fujishima, A.; Honda, K. Electrochemical Photolysis of Water at a Semiconductor Electrode. *Nature* **1972**, *238* (5358), 37−38.

(2) Lau, V. W.-h.; Moudrakovski, I.; Botari, T.; Weinberger, S.; Mesch, M. B.; Duppel, V.; Senker, J.; Blum, V.; Lotsch, B. V. Rational Design of Carbon Nitride Photocatalysts by Identification of Cyanamide Defects as Catalytically Relevant Sites. *Nat. Commun.* **2016**, *7*, 12165.

(3) Dhakshinamoorthy, A.; Asiri, A. M.; García, H. Metal-Organic Framework (MOF) Compounds: Photocatalysts for Redox Reactions and Solar Fuel Production. *Angew. Chem., Int. Ed.* **2016**, *55* (18), 5414−5445.

(4) Cao, S.; Low, J.; Yu, J.; Jaroniec, M. Polymeric Photocatalysts Based on Graphitic Carbon Nitride. *Adv. Mater.* **2015**, *27* (13), 2150−2176.

(5) Asahi, R.; Morikawa, T.; Irie, H.; Ohwaki, T. Nitrogen-Doped Titanium Dioxide as Visible-Light-Sensitive Photocatalyst: Designs,

Developments, and Prospects. *Chem. Rev.* **2014**, *114* (19), 9824−9852.
(6) Zhang, Q.; Deng, J.; Xu, Z.; Chaker, M.; Ma, D. High-Efficiency Broadband C_3N_4 Photocatalysts: Synergistic Effects from Upconversion and Plasmons. *ACS Catal.* **2017**, *7* (9), 6225−6234.
(7) Liao, G.; Gong, Y.; Zhang, L.; Gao, H.; Yang, G.-J.; Fang, B. Semiconductor Polymeric Graphitic Carbon Nitride Photocatalysts: The "Holy Grail" for the Photocatalytic Hydrogen Evolution Reaction under Visible Light. *Energy Environ. Sci.* **2019**, *12* (7), 2080−2147.
(8) Tay, Q.; Kanhere, P.; Ng, C. F.; Chen, S.; Chakraborty, S.; Huan, A. C. H.; Sum, T. C.; Ahuja, R.; Chen, Z. Defect Engineered g-C_3N_4 for Efficient Visible Light Photocatalytic Hydrogen Production. *Chem. Mater.* **2015**, *27* (14), 4930−4933.
(9) Ye, C.; Li, J.-X.; Li, Z.-J.; Li, X.-B.; Fan, X.-B.; Zhang, L.-P.; Chen, B.; Tung, C.-H.; Wu, L.-Z. Enhanced Driving Force and Charge Separation Efficiency of Protonated g-C_3N_4 for Photocatalytic O_2 Evolution. *ACS Catal.* **2015**, *5* (11), 6973−6979.
(10) Zada, A.; Humayun, M.; Raziq, F.; Zhang, X.; Qu, Y.; Bai, L.; Qin, C.; Jing, L.; Fu, H. Exceptional Visible-Light-Driven Cocatalyst-Free Photocatalytic Activity of g-C_3N_4 by Well Designed Nanocomposites with Plasmonic Au and SnO_2. *Adv. Energy Mater.* **2016**, *6* (21), 1601190.
(11) Xu, H.; Yan, J.; Xu, Y.; Song, Y.; Li, H.; Xia, J.; Huang, C.; Wan, H. Novel Visible-Light-Driven AgX/Graphite-Like C_3N_4 (X = Br, I) Hybrid Materials with Synergistic Photocatalytic Activity. *Appl. Catal., B* **2013**, *129*, 182−193.
(12) Zhang, G.; Lan, Z.-A.; Lin, L.; Lin, S.; Wang, X. Overall Water Splitting by Pt/g-C_3N_4 Photocatalysts without Using Sacrificial Agents. *Chem. Sci.* **2016**, *7* (5), 3062−3066.
(13) Liu, J.; Yang, Y.; Liu, N.; Liu, Y.; Huang, H.; Kang, Z. Total Photocatalysis Conversion from Cyclohexane to Cyclohexanone by C_3N_4/Au Nanocomposites. *Green Chem.* **2014**, *16* (10), 4559−4565.
(14) Kong, H. J.; Won, D. H.; Kim, J.; Woo, S. I. Sulfur-Doped g-C_3N_4/$BiVO_4$ Composite Photocatalyst for Water Oxidation under Visible Light. *Chem. Mater.* **2016**, *28* (5), 1318−1324.
(15) Tan, X.; Tahini, H. A.; Smith, S. C. P-Doped Graphene/Graphitic Carbon Nitride Hybrid Electrocatalysts: Unraveling Charge Transfer Mechanisms for Enhanced Hydrogen Evolution Reaction Performance. *ACS Catal.* **2016**, *6* (10), 7071−7077.
(16) Huang, Z.-F.; Song, J.; Pan, L.; Wang, Z.; Zhang, X.; Zou, J.-J.; Mi, W.; Zhang, X.; Wang, L. Carbon Nitride with Simultaneous Porous Network and O-Doping for Efficient Solar-Energy-Driven Hydrogen Evolution. *Nano Energy* **2015**, *12*, 646−656.
(17) Linic, S.; Christopher, P.; Ingram, D. B. Plasmonic-Metal Nanostructures for Efficient Conversion of Solar to Chemical Energy. *Nat. Mater.* **2011**, *10* (12), 911−921.
(18) Wang, F.; Jiang, Y.; Lawes, D. J.; Ball, G. E.; Zhou, C.; Liu, Z.; Amal, R. Analysis of the Promoted Activity and Molecular Mechanism of Hydrogen Production over Fine Au-Pt Alloyed TiO_2 Photocatalysts. *ACS Catal.* **2015**, *5* (7), 3924−3931.
(19) Tan, T. H.; Scott, J.; Ng, Y. H.; Taylor, R. A.; Aguey-Zinsou, K.-F.; Amal, R. Understanding Plasmon and Band Gap Photoexcitation Effects on the Thermal-Catalytic Oxidation of Ethanol by TiO_2-Supported Gold. *ACS Catal.* **2016**, *6* (3), 1870−1879.
(20) Zhang, Q.; Thrithamarassery Gangadharan, D.; Liu, Y.; Xu, Z.; Chaker, M.; Ma, D. Recent Advancements in Plasmon-Enhanced Visible Light-Driven Water Splitting. *J. Materiomics* **2017**, *3* (1), 33−50.
(21) Clavero, C. Plasmon-Induced Hot-Electron Generation at Nanoparticle/Metal-Oxide Interfaces for Photovoltaic and Photocatalytic Devices. *Nat. Photonics* **2014**, *8* (2), 95−103.
(22) Christopher, P.; Xin, H.; Linic, S. Visible-Light-Enhanced Catalytic Oxidation Reactions on Plasmonic Silver Nanostructures. *Nat. Chem.* **2011**, *3* (6), 467−472.
(23) Mateo, D.; Esteve-Adell, I.; Albero, J.; Royo, J. F. S.; Primo, A.; Garcia, H. 111 Oriented Gold Nanoplatelets on Multilayer Graphene as Visible Light Photocatalyst for Overall Water Splitting. *Nat. Commun.* **2016**, *7*, 11819.
(24) Bai, J.; Lu, B.; Han, Q.; Li, Q.; Qu, L. (111) Facets-Oriented Au-Decorated Carbon Nitride Nanoplatelets for Visible-Light-Driven Overall Water Splitting. *ACS Appl. Mater. Interfaces* **2018**, *10* (44), 38066−38072.
(25) Bamwenda, G. R.; Tsubota, S.; Nakamura, T.; Haruta, M. The Influence of the Preparation Methods on the Catalytic Activity of Platinum and Gold Supported on TiO_2 for CO Oxidation. *Catal. Lett.* **1997**, *44* (1−2), 83−87.
(26) Haruta, M.; Yamada, N.; Kobayashi, T.; Iijima, S. Gold Catalysts Prepared by Coprecipitation for Low-Temperature Oxidation of Hydrogen and of Carbon Monoxide. *J. Catal.* **1989**, *115* (2), 301−309.
(27) Golunski, S.; Rajaram, R.; Hodge, N.; Hutchings, G. J.; Kiely, C. J. Low-Temperature Redox Activity in Co-Precipitated Catalysts: A Comparison between Gold and Platinum-Group Metals. *Catal. Today* **2002**, *72* (1−2), 107−113.
(28) Riahi, G.; Guillemot, D.; Polisset-Thfoin, M.; Khodadadi, A. A.; Fraissard, J. Preparation, Characterization and Catalytic Activity of Gold-Based Nanoparticles on HY Zeolites. *Catal. Today* **2002**, *72* (1−2), 115−121.
(29) Okumura, M.; Nakamura, S.; Tsubota, S.; Nakamura, T.; Azuma, M.; Haruta, M. Chemical Vapor Deposition of Gold on Al_2O_3, SiO_2, and TiO_2 for the Oxidation of CO and of H_2. *Catal. Lett.* **1998**, *51* (1−2), 53−58.
(30) Zhu, J.; Fan, F.; Chen, R.; An, H.; Feng, Z.; Li, C. Direct Imaging of Highly Anisotropic Photogenerated Charge Separations on Different Facets of a Single $BiVO_4$ Photocatalyst. *Angew. Chem., Int. Ed.* **2015**, *54* (31), 9111−9114.
(31) Mu, L.; et al. Enhancing Charge Separation on High Symmetry $SrTiO_3$ Exposed with Anisotropic Facets for Photocatalytic Water Splitting. *Energy Environ. Sci.* **2016**, *9* (7), 2463−2469.
(32) Yu, H.; Cao, C.; Wang, X.; Yu, J. Ag-Modified BiOCl Single-Crystal Nanosheets: Dependence of Photocatalytic Performance on the Region-Selective Deposition of Ag Nanoparticles. *J. Phys. Chem. C* **2017**, *121* (24), 13191−13201.
(33) Wenderich, K.; Mul, G. Methods, Mechanism, and Applications of Photodeposition in Photocatalysis: A Review. *Chem. Rev.* **2016**, *116* (23), 14587−14619.
(34) Li, L.; Zhang, J.; Zhang, Q.; Wang, X.; Dai, W.-L. Superior Sponge-Like Carbon Self-Doping g-C_3N_4 Nanosheets Derived from Supramolecular Pre-Assembly of Melamine-Cyanuric Acid Complex for Photocatalytic H_2 Evolution. *Nanotechnology* **2021**, *32* (15), 155604.
(35) Samanta, S.; Martha, S.; Parida, K. Facile Synthesis of Au/g-C_3N_4 Nanocomposites: An Inorganic/Organic Hybrid Plasmonic Photocatalyst with Enhanced Hydrogen Gas Evolution under Visible-Light Irradiation. *ChemCatChem* **2014**, *6* (5), 1453−1462.
(36) Gao, H.; Cao, R.; Zhang, S.; Yang, H.; Xu, X. Three-Dimensional Hierarchical g-C_3N_4 Architectures Assembled by Ultrathin Self-Doped Nanosheets: Extremely Facile Hexamethylenetetramine Activation and Superior Photocatalytic Hydrogen Evolution. *ACS Appl. Mater. Interfaces* **2019**, *11* (2), 2050−2059.
(37) Yu, H.; Shi, R.; Zhao, Y.; Bian, T.; Zhao, Y.; Zhou, C.; Waterhouse, G. I. N.; Wu, L.-Z.; Tung, C.-H.; Zhang, T. Alkali-Assisted Synthesis of Nitrogen Deficient Graphitic Carbon Nitride with Tunable Band Structures for Efficient Visible-Light-Driven Hydrogen Evolution. *Adv. Mater.* **2017**, *29* (16), 1605148.
(38) Fang, Z.; Hong, Y.; Li, D.; Luo, B.; Mao, B.; Shi, W. One-Step Nickel Foam Assisted Synthesis of Holey G-Carbon Nitride Nanosheets for Efficient Visible-Light Photocatalytic H_2 Evolution. *ACS Appl. Mater. Interfaces* **2018**, *10* (24), 20521−20529.
(39) Martha, S.; Reddy, K. H.; Biswal, N.; Parida, K. Facile Synthesis of Ingazn Mixed Oxide Nanorods for Enhanced Hydrogen Production under Visible Light. *Dalton T.* **2012**, *41* (46), 14107−14116.
(40) Wang, X.; Andrews, L. Infrared Spectra and Structures of the Coinage Metal Dihydroxide Molecules. *Inorg. Chem.* **2005**, *44* (24), 9076−9083.
(41) Cheng, W.; et al. Synergetic Enhancement of Plasmonic Hot-Electron Injection in Au Cluster-Nanoparticle/C_3N_4 for Photo-

https://doi.org/10.1021/acs.jpcc.1c02269
J. Phys. Chem. C 2021, 125, 10964−10973

catalytic Hydrogen Evolution. *J. Mater. Chem. A* **2017**, *5* (37), 19649−19655.
(42) Johnson, C. J.; Dujardin, E.; Davis, S. A.; Murphy, C. J.; Mann, S. Growth and Form of Gold Nanorods Prepared by Seed-Mediated, Surfactant-Directed Synthesis. *J. Mater. Chem.* **2002**, *12* (6), 1765−1770.
(43) Wang, X.; Maeda, K.; Chen, X.; Takanabe, K.; Domen, K.; Hou, Y.; Fu, X.; Antonietti, M. Polymer Semiconductors for Artificial Photosynthesis: Hydrogen Evolution by Mesoporous Graphitic Carbon Nitride with Visible Light. *J. Am. Chem. Soc.* **2009**, *131* (5), 1680−1681.
(44) Zhou, X.; Jin, B.; Li, L.; Peng, F.; Wang, H.; Yu, H.; Fang, Y. A Carbon Nitride/TiO_2 Nanotube Array Heterojunction Visible-Light Photocatalyst: Synthesis, Characterization, and Photoelectrochemical Properties. *J. Mater. Chem.* **2012**, *22* (34), 17900−17905.
(45) Martha, S.; Nashim, A.; Parida, K. M. Facile Synthesis of Highly Active g-C_3N_4 for Efficient Hydrogen Production under Visible Light. *J. Mater. Chem. A* **2013**, *1* (26), 7816−7824.
(46) Dong, F.; Wu, L.; Sun, Y.; Fu, M.; Wu, Z.; Lee, S. C. Efficient Synthesis of Polymeric g-C_3N_4 Layered Materials as Novel Efficient Visible Light Driven Photocatalysts. *J. Mater. Chem.* **2011**, *21* (39), 15171−15174.
(47) Dozzi, M. V.; Prati, L.; Canton, P.; Selli, E. Effects of Gold Nanoparticles Deposition on the Photocatalytic Activity of Titanium Dioxide under Visible Light. *Phys. Chem. Chem. Phys.* **2009**, *11* (33), 7171−7180.
(48) Veith, G. M.; Lupini, A. R.; Dudney, N. J. Role of pH in the Formation of Structurally Stable and Catalytically Active TiO_2-Supported Gold Catalysts. *J. Phys. Chem. C* **2009**, *113* (1), 269−280.
(49) Wang, M.; Cai, L.; Wang, Y.; Zhou, F.; Xu, K.; Tao, X.; Chai, Y. Graphene-Draped Semiconductors for Enhanced Photocorrosion Resistance and Photocatalytic Properties. *J. Am. Chem. Soc.* **2017**, *139* (11), 4144−4151.

https://doi.org/10.1021/acs.jpcc.1c02269
J. Phys. Chem. C 2021, 125, 10964−10973